Obrabotka metallov (tekhnologiya, oborudovanie, instrumenty) = Metal Working and Material Science. 2026 vol. 28 no. 2 pp. 243–263
ISSN: 1994-6309 (print) / 2541-819X (online)
DOI: 10.17212/1994-6309-2026-28.2-243-263

NSTU NETI

Obrabotka metallov - Metal Working and Material Science

Journal homepage: http://journals.nstu.ru/obrabotka_metallov

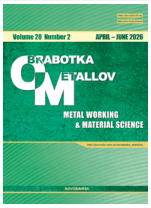

Study of the microstructure and properties of high-entropy alloy AlFeCoCrNiNb$_x$ fabricated by mechanical alloying and spark plasma sintering

Yuanxun Liu [1, b], *Zhanna Kovalevskaya* [1, a, *], *Jingrui Huang* [1, c], *Margarita Khimich* [2, d]

[1] National Research Tomsk Polytechnic University, 30 Lenin Avenue, Tomsk, 634050, Russian Federation
[2] Institute of Strenght Physics and Materials Sciences SB RAS, 2/4 per. Academicheskii, Tomsk, 634055, Russian Federation

[a] https://orcid.org/0009-0002-8501-2643, yuansyun1@tpu.ru; [b] https://orcid.org/0000-0003-3040-8851, kovalevskaya@tpu.ru;
[c] https://orcid.org/0000-0003-1070-7678, jereehuang@gmail.com; [d] https://orcid.org/0000-0001-5859-7418, khimich@ispms.ru

ARTICLE INFO

Article history:
Received: 27 January 2026
Revised: 02 February 2026
Accepted: 14 March 2026
Available online: 15 June 2026

Keywords:
High-Entropy Alloy
AlFeCoCrNiNb$_x$
Mechanical alloying
Spark plasma sintering
Microstructure
Microhardness
Compression Tests

Funding
The study was supported by the Russian Science Foundation, Project No. 25-49-00169, https://rscf.ru/project/25-49-00169/.

ABSTRACT

Introduction. Mechanical alloying (*MA*) combined with spark plasma sintering (*SPS*) is widely used for the fabrication of high-entropy alloys (*HEAs*). The combination of *MA* and *SPS* effectively suppresses grain growth, largely preserving the structure obtained after mechanical activation. This enables the production of *HEAs* with unique properties. In this study, *HEAs* of the *AlFeCoCrNiNb$_x$* system (where x is the molar fraction, x = 0, 0.25, 0.5, and 0.75) were fabricated by *MA* for 40 hours followed by *SPS* at 1,000 °C. ***The purpose of this work*** is to investigate the effect of *Nb* content on the microstructure and properties of the *AlFeCoCrNiNb$_x$* high entropy alloy obtained via the combined *MA* and *SPS* method. **Methods.** Both initial powders and sintered samples were studied by X-ray diffraction (*XRD*), energy-dispersive X-ray spectroscopy (*EDS*), and scanning electron microscopy (*SEM*). Microhardness and compressive properties were evaluated, and the resulting fracture surfaces were analyzed. **Results and Discussion.** During *MA*, a solid solution with a *BCC* lattice and a nanoscale substructure was formed in the powder of all *AlFeCoCrNiNb$_x$* alloys. Alloying with a significant fraction of niobium led to the formation of a small amount of the strengthening *Laves* phase. Subsequent *SPS* promoted a phase transformation, resulting in approximately equal volume fractions of a *BCC* solid solution enriched in *Al* and *Ni* and an *FCC* solid solution enriched in *Fe* and *Cr*. Heating facilitated the precipitation of the *Laves* phase as secondary grains within the *BCC* solid solution grains. Increasing the *Nb* content in the alloy led to an increase in the fraction of the *Laves* phase. Evaluation of the mechanical properties showed that the highest plasticity is characteristic of the *AlFeCoCrNi* alloy; the highest strength, of the *AlFeCoCrNiNb$_{0.25}$* alloy; the highest hardness, of the *AlFeCoCrNiNb$_{0.75}$* alloy, which is attributed to the specific microstructural features and the fraction of the *Laves* phase in the alloy.

For citation: Liu Y., Kovalevskaya Z.G., Huang J., Khimich M.A. Study of the microstructure and properties of high-entropy alloy AlFeCoCrNiNb$_x$ fabricated by mechanical alloying and spark plasma sintering. *Obrabotka metallov (tekhnologiya, oborudovanie, instrumenty) = Metal Working and Material Science*, 2026, vol. 28, no. 2, pp. 243–263. DOI: 10.17212/1994-6309-2026-28.2-243-263. (In Russian).

Introduction

In 2004, *J. W. Yeh* and his colleagues pioneered a novel alloy design paradigm by introducing high-entropy alloys (*HEAs*) [1, 2]. Conventionally defined as systems comprising five or more principal elements in near-equimolar ratios with minimal atomic radius disparities, *HEAs* were originally hypothesized to stabilize as single-phase, disordered solid solutions. This stabilization arises from their high configurational entropy, which favors the formation of crystal lattices that are energetically optimal for the entire system [3]. However, contemporary research has shifted away from the initial pursuit of strictly single-phase

*** Corresponding author**
Kovalevskaya Zhanna G., D.Sc. (Engineering), Professor
National Research Tomsk Polytechnic University,
30 Lenin Avenue,
634050, Tomsk, Russian Federation
Tel.: +7 906 199-05-77, **e-mail:** kovalevskaya@tpu.ru

microstructures, recognizing that such constraints significantly limit the tunability of both structure and properties [4, 5]. Instead, by strategically adjusting elemental ratios or incorporating additional alloying constituents, researchers can induce profound phase transformations and microstructural evolutions. These deliberate modifications enable the precise tailoring of mechanical performance and service characteristics, thereby unlocking the full potential of these advanced materials [6–9].

Within the extensive family of high-entropy alloys (*HEAs*), the *AlFeCoCrNi* system, characterized by a body-centered cubic (*BCC*) lattice, has garnered significant research attention [10–12]. A pivotal strategy for optimizing the strength–ductility synergy in this alloy involves the introduction of a fifth constituent, such as *Ti*, *Zr*, or *V* [12]. Such alloying elements can fundamentally alter either the phase constitution or the lattice parameters of the primary matrix. For instance, investigations on *Ti* [13] and *Zr* [14] additions reveal that both elements promote the precipitation of the *Laves* phase, thereby substantially modifying the suite of physicomechanical properties. Specifically, superior compressive mechanical properties were exhibited by *Ti*-alloyed $AlCoCrFeNiTi_{0.5}$ ($\boldsymbol{\sigma_{0.2}}$ = 2,260 MPa, $\boldsymbol{\sigma_u}$ = 3,140 MPa, $\boldsymbol{\varepsilon}$ = 23.3%) [13] and by *Zr*-modified $AlCrCoNiFeZr_{0.008}$ ($\boldsymbol{\sigma_{0.2}}$ = 1,560 MPa, $\boldsymbol{\sigma_u}$ = 3513 MPa, $\boldsymbol{\varepsilon}$ = 29.5%) [14]. In both instances, enhanced mechanical characteristics are typical of hypoeutectic microstructures comprising solid solution grains interspersed with a eutectic mixture of solid solution and the *Laves* phase. Conversely, the vanadium (*V*) addition was observed to preserve the original phase composition [15]. Instead, *V* atoms completely dissolved into the solid solution matrix, distorting the lattice parameters and thereby enhancing mechanical performance. The most favorable properties were observed in *AlCoCrFeNiV* ($\boldsymbol{\sigma_{0.2}}$ = 1726.5 MPa, ***HV*** = 6,488 MPa) and $AlCoCrFeNiV_{0.2}$ ($\boldsymbol{\sigma_u}$ = 3,297.8 MPa, $\boldsymbol{\varepsilon}$ = 26.8%) [15].

Niobium (*Nb*) alloying induces analogous phase and structural transformations. Given its larger atomic radius relative to the other constituents, *Nb* causes severe lattice distortions, thereby significantly enhancing alloy strength. Furthermore, niobium exhibits a negative enthalpy of mixing with the matrix elements, which thermodynamically favors the formation of hexagonal close-packed (*HCP*) *Laves* phases and drives the microstructural evolution toward a eutectic architecture [16]. While introducing a substantial fraction of *Nb* typically compromises ductility, identifying the optimal *Nb* concentration allows for a significant enhancement in strength without sacrificing adequate plasticity. In the as-cast state, an optimal balance of properties was achieved in the $AlCrCoNiFeNb_{0.25}$ alloy ($\boldsymbol{\sigma_{0.2}}$ = 1,959 MPa, $\boldsymbol{\sigma_u}$ = 3,008 MPa, $\boldsymbol{\varepsilon}$ = 10.5%, ***HV*** = 6,680 MPa) [17]. Additionally, as demonstrated in our previous work, appropriate heat treatment can facilitate further advantageous phase and structural transformations [18].

Currently, high-entropy alloys (*HEAs*) are predominantly synthesized via arc melting and vacuum induction melting [19]. However, alloys produced through these conventional methods are prone to macroscopic segregation, often resulting in a significant discrepancy between theoretical predictions and actual material properties. Consequently, mechanical alloying (*MA*) has emerged as a critical alternative processing technique to complement traditional methods [20, 21]. Furthermore, the consolidation of *HEA* powders via spark plasma sintering (*SPS*) enables the fabrication of materials possessing a unique synergy of properties [19, 22–23]. The paramount advantage of *MA* lies in its ability to enhance elemental solubility and thermodynamically drive the formation of supersaturated solid solutions. For instance, a study on *AlCoCrFeNi* powders subjected to *MA* investigated phase evolution as a function of milling duration [24]. Prolonged milling was observed to induce continuous grain refinement, suppress the *FCC* phase in favor of its dissolution into the *BCC* matrix, and exacerbate lattice distortion. A homogeneous single-phase solid solution was achieved after 30 hours of milling, a finding corroborated by subsequent studies [25, 26]. The optimal milling duration is governed by key operational parameters, including the rotational speed of the planetary mill (typically ranging from 250 to 400 rpm) and the ball-to-powder mass ratio (e.g., 7:1, 10:1, or 15:1). Through the precise optimization of these variables, *MA* can successfully yield a single-phase nanocrystalline microstructure in the *AlFeCoCrNi* system [21–26].

The subsequent *SPS* process, characterized by the synergistic application of pulsed electric current, rapid heating rates, and uniaxial pressure, facilitates accelerated atomic diffusion at the localized contact interfaces between consolidating particles [19]. In the context of the *AlFeCoCrNi* system, the high kinetics of *SPS* enables the retention of metastable phases and portions of an ultrafine-grained microstructure rich

in crystallographic defects [22]. This resulting architecture stands in stark contrast to the coarse-grained structures typically obtained via conventional sintering methods, as documented in previous studies [25]. Notably, *SPS* was observed to induce a partial transformation of the *BCC* phase into an *FCC* phase, a transition that significantly enhances the alloy's mechanical performance. However, the fate of the residual *BCC* phase remains a subject of investigation. While some research suggests its reconstruction into a *B2* ordered superlattice (an *AlNi*-based variant of the *BCC* structure) [24], it is crucial to acknowledge that standard X-ray diffraction (*XRD*) techniques often fail to distinguish between disordered *BCC* and ordered *B2* phases due to their similar scattering patterns [22].

In the present study, high-entropy alloys (*HEAs*) of the $AlFeCoCrNiNb_x$ system, with molar fractions of $\boldsymbol{x}$ = 0, 0.25, 0.5, and 0.75, were synthesized via mechanical alloying (*MA*) for 40 hours, followed by consolidation using *SPS* at 1,000 °C. This work systematically investigates the influence of niobium content on the mechanical alloying kinetics, the resulting microstructural evolution, and the final mechanical properties of the alloys after *SPS*.

The primary aim of this study is to investigate the influence of *Nb* content on the microstructure and properties of $AlFeCoCrNiNb_x$ high-entropy alloys (*HEAs*) synthesized via a combined approach of mechanical alloying (*MA*) followed by *SPS*. To achieve this aim, the following specific ***tasks*** were defined:

– to characterize powder precursors: to examine the structural-phase state and external morphology of $AlCoCrFeNiNb_x$ alloy powders produced by *MA*;

– to analyze consolidation transformations: to describe the phase and structural transformations occurring within the alloys during the *SPS* consolidation process;

– to evaluate mechanical performance: to assess the mechanical properties through compression testing and microhardness measurements;

– to establish structure–property correlations: to determine the relationship between the evolved microstructures and the resulting properties of the investigated alloys.

Methods

High-purity (99.9%) elemental powders of *Al*, *Co*, *Cr*, *Fe*, *Ni*, and *Nb*, with an average particle size of 50 μm, served as the starting materials. High-entropy alloys (*HEAs*) with the $AlFeCoCrNiNb_x$ composition (where $\boldsymbol{x}$ denotes the molar fraction, $\boldsymbol{x}$ = 0, 0.25, 0.5, 0.75) were synthesized via mechanical alloying (*MA*). For brevity, the resulting samples are designated as *Nb0*, *Nb0.25*, *Nb0.5*, and *Nb0.75*, corresponding to their respective *Nb* molar fractions. This compositional range was selected based on the reported solubility limit of *Nb* in the *AlCoCrFeNi* solid solution, which is less than 4.76 at.% (equivalent to $\boldsymbol{x}$ = 0.25) [17]. Within this limit, *Nb* is expected to dissolve completely in the matrix during *MA*, contributing to strengthening primarily through a solid-solution mechanism. However, exceeding the critical concentration of $\boldsymbol{x}$ = 0.25 promotes the formation of a strengthening *Laves* phase. Given the scarcity of literature detailing the influence of excess *Nb* on the microstructural evolution of these alloys during both *MA* and subsequent *SPS* consolidation, investigating the *AlCoCrFeNi* system alloyed with *Nb* molar fractions ranging from 0.25 to 0.75 is of considerable scientific interest [27].

Milling was conducted using a *QM-3SP4* planetary ball mill equipped with stainless steel (*SUS316*) jars and balls. The chemical composition of the milling media (comprising primarily *Fe* with 16–18 wt.% *Cr* and 13–15 wt.% *Ni*, alongside a negligible carbon content (0.03 wt.%)) precisely matches the composition of the target alloy, minimizing external impurities. To preclude oxidation during *MA*, the jars were subjected to repeated vacuum cycles before being backfilled with high-purity argon for the whole process. Stearic acid (3 wt.%) was employed as a process control agent to mitigate agglomeration. Milling was optimized with a ball-to-powder mass ratio of 10:1, a rotational speed of 300 rpm, and a total milling duration of 40 hours. Upon completion, the resultant powder was sieved through a 75 μm mesh to obtain the final product.

The synthesized alloy powders were consolidated via spark plasma sintering (*SPS*) using graphite dies, punches, and spacer sheets. The entire sintering cycle was conducted under vacuum conditions with a heating rate of 100 °C/min. Upon reaching 1,000 °C, a uniaxial pressure of 50 MPa was applied and

maintained for 15 minutes, followed by furnace cooling. Real-time data logging captured the evolution of temperature, pressure, and punch displacement throughout the *SPS* process. The resulting consolidated billets were cylindrical, measuring 20 mm in diameter and 7 mm in thickness. Specimens of appropriate geometry were subsequently machined from these billets for subsequent characterization and testing.

X-ray diffraction (*XRD*) analyses were performed on both the as-milled powders and sintered specimens using an *XRD-6000* diffractometer equipped with *Cu-Kα* radiation. Scans were acquired over a 2θ range of 10°–90° with a step size of 0.02°. Diffraction patterns were utilized to derive key structural parameters: the crystallite size and microstrain were estimated via the *Scherrer* method, while lattice parameters and phase fractions were quantified through *Rietveld* refinement. Elemental composition was determined by local energy-dispersive X-ray spectroscopy (*EDS*) in combination with scanning electron microscopy (*SEM*) (*JEOL JSM6000 NEJSCOP*). Microstructural characterization of polished and etched (with aqua regia) samples was conducted using *SEM*. Bulk density and porosity were evaluated via the *Archimedes* principle (hydrostatic weighing). Room-temperature compressive mechanical properties were assessed using an *Instron 5500* testing system at a strain rate of 1×10^{-3} s^{-1}, employing rectangular parallelepiped specimens ($4 \times 4 \times 7$ mm^3); at least three replicates were tested for each alloy composition to ensure statistical reliability. *Vickers* microhardness measurements were carried out on a *PMT-3* microhardness tester under a 500 g load in accordance with standard protocols. For all reported mechanical properties, values are presented as means accompanied by their respective standard deviations.

Results and discussion

Table 1 presents the results of elemental analysis performed via energy-dispersive X-ray spectroscopy (*EDS*). The data indicate that the chemical composition of the alloys, both after mechanical alloying (*MA*) and subsequent spark plasma sintering (*SPS*), aligns closely with the target atomic percentages.

The obtained data indicate that the alloy composition, both after *MA* and *SPS*, generally aligns with the expected atomic percentages, albeit with minor discrepancies. These variations in elemental content between the initial powder mixtures and the consolidated specimens can be attributed to the specific nature of the data acquisition methods. For the powders, measurements were taken from particle surfaces, whereas for the consolidated material, analysis was performed on cross-sections, representing the interior. It is plausible that during *MA*, the surface layer of particles develops a composition distinct from the core material due to the specific mechanisms governing their formation.

Fig. 1 displays scanning electron microscopy (*SEM*) micrographs and the corresponding *EDS* results for the alloy powders synthesized via *MA*.

Table 1

Chemical composition of *AlFeCoCrNiNb$_x$* alloys (at. %)

Alloy	Condition	*Al*	*Fe*	*Cr*	*Co*	*Ni*	*Nb*
Nb0	Designation	20	20	20	20	20	0
	Powder	24.0	18.3	19.4	18.7	19.6	0
	SPS	24.9	18.4	17.7	19.0	20.0	0
Nb0.25	Designation	19.1	19.1	19.1	19.1	19.1	4.5
	Powder	19.2	19.6	17.2	21.3	18.2	4.5
	SPS	21.3	18.1	18.0	18.2	20.0	4.4
Nb0.5	Designation	18.2	18.2	18.2	18.2	18.2	9.0
	Powder	17.4	18.4	17.6	19.8	17.9	8.9
	SPS	19.8	17.4	17.9	17.3	18.8	8.8
Nb0.75	Designation	17.4	17.4	17.4	17.4	17.4	13.0
	Powder	17.7	17.6	16.7	17.8	17.7	12.5
	SPS	22.3	15.7	16.1	15.9	17.8	12.2

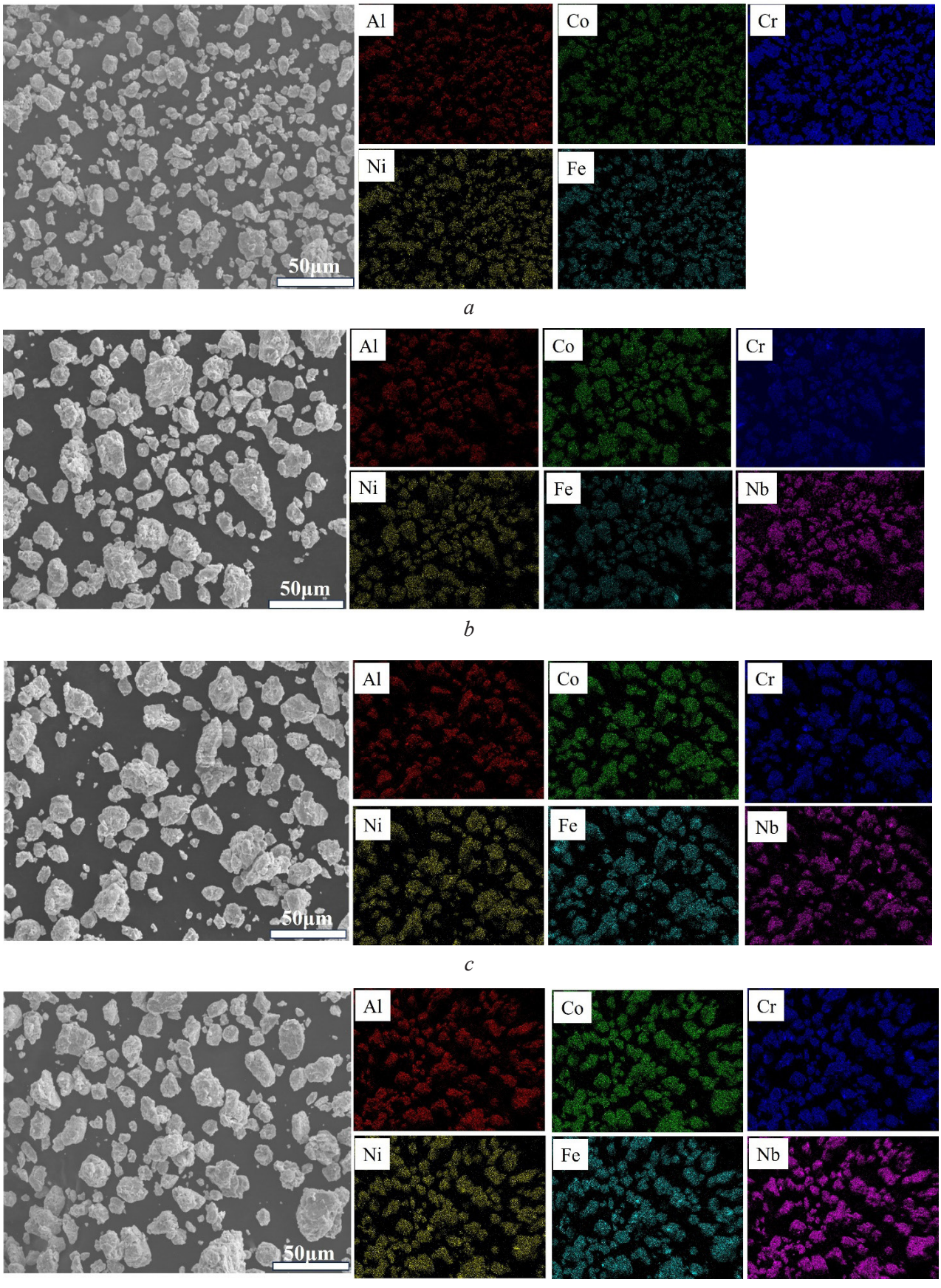

Fig. 1. SEM images and *EDS* results of $AlFeCoCrNiNb_x$ powders produced by *MA*:
a – Nb0; *b – Nb0.25*; *c – Nb0.5*; *d – Nb0.75*

During *MA*, continuous collisions between powder particles of the initial components lead to their fracture and refinement. Plastic deformation of the particles increases the density of crystal lattice defects, such as dislocations and point defects, thereby enhancing interdiffusion of the components into each other's lattices. The reduction in particle size increases their specific surface area and, consequently, their surface energy, making the powder prone to agglomeration and cold welding [20]. After 40 hours of repeated cycles of plastic deformation, fragmentation, agglomeration, and cold welding, the particle size and morphology stabilize. The particles become slightly smaller than the initial ones and exhibit a uniform shape. *EDS* results reveal a homogeneous distribution of all alloy components within the powder (Fig. 1), indicating that the prolonged *MA* process successfully ensures material homogeneity.

Fig. 2 presents the results of granulometric analysis of the powders, performed using *ImageJ* software. The particle size distribution is narrow, which enhances flowability and provides a favorable basis for producing specimens via *SPS*. All calculated characteristics – $\boldsymbol{D}_{\text{average}}$ (average particle size), $\boldsymbol{D}_{50}$ (the size below which 50% of the particles fall), and $\boldsymbol{D}_{90}$ (the size below which 90% of the particles fall) – are smaller for the *Nb*-free powder compared to the *Nb*-alloyed powders. Specifically, the particle size of the *Nb0* alloy powder ranges up to 21 μm, whereas for the *Nb0.25*, *Nb0.5*, and *Nb0.75* alloys, it extends up to 35 μm. The primary reason for the increased size of the alloyed particles is that *Nb*, being a softer metal, acts as a binder during the mechanical activation process, thereby intensifying agglomeration.

X-ray diffraction patterns of the $AlFeCoCrNiNb_x$ powders for all investigated compositions after 40 hours of *MA* show no peaks corresponding to the initial elemental components (Fig. 3) [28]. The following phases form in the obtained material. The primary phase for all alloy compositions is a *BCC* phase, representing a

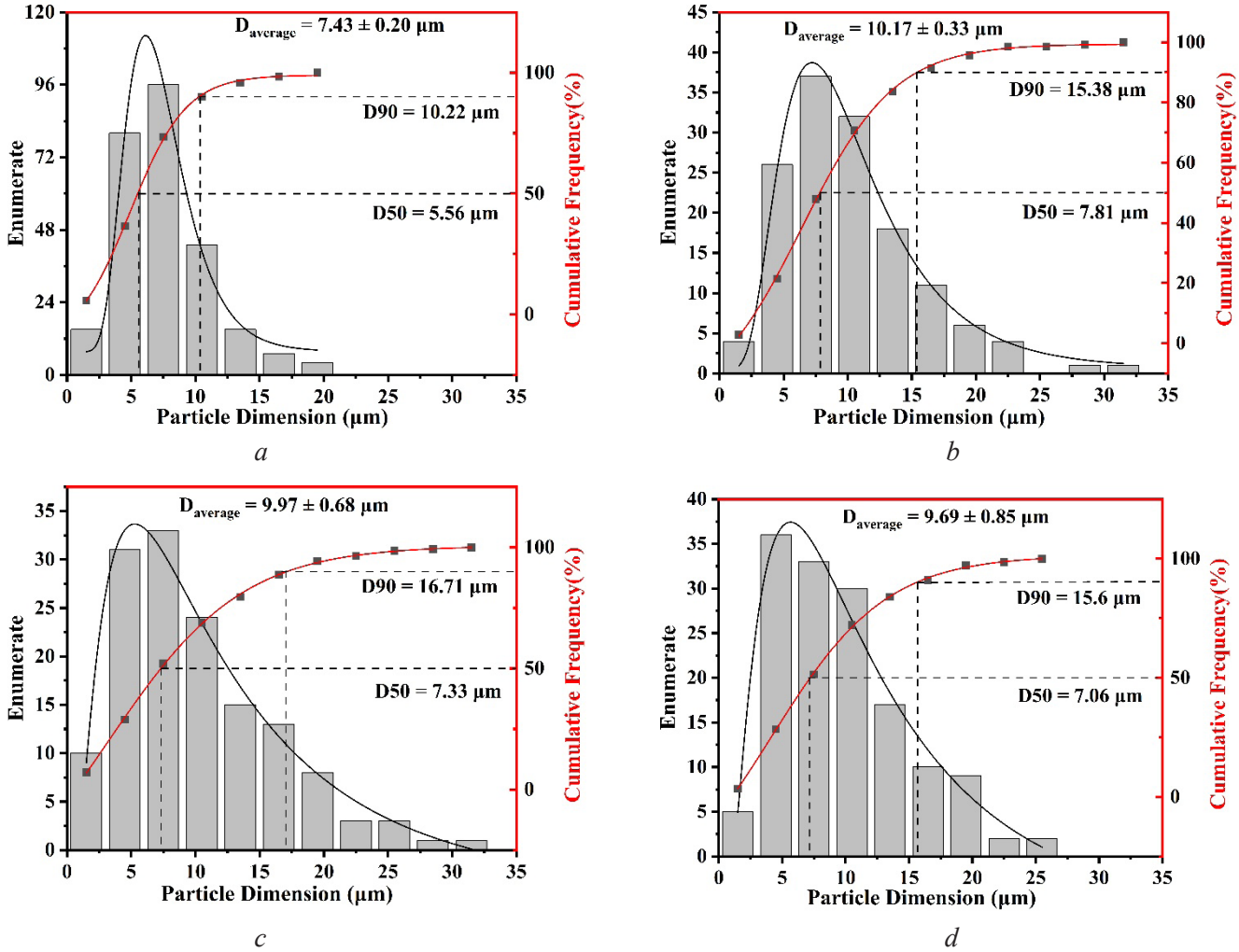

Fig. 2. Particle size distribution of $AlFeCoCrNiNb_x$ powders produced by *MA*:
a – Nb0; *b – Nb0.25*; *c – Nb0.5*; *d – Nb0.75*

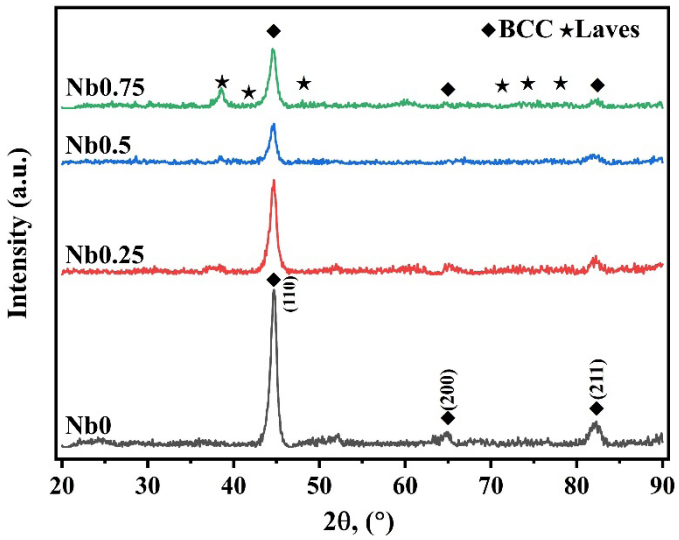

Fig. 3. XRD patterns of $AlFeCoCrNiNb_x$ powders produced by *MA*

disordered solid solution of all components present in the system. Additionally, in the *Nb*-alloyed alloys, a *Laves* phase is identified. In this case, it is a complex intermetallic compound described as $(CoCr)_2Nb$ with a hexagonal crystal lattice [16]. Analysis of the effect of *Nb* content on the phase composition reveals that, in the *Nb0.25*, *Nb0.5*, and *Nb0.75* powders, the intensity of the diffraction peaks corresponding to the *Laves* phase increases at a higher *Nb* content. This indicates a trend toward an increased volume fraction of the *Laves* phase within the alloy structure as the *Nb* concentration rises.

Table 2 presents the calculated structural parameters of the *BCC* phase in the powders obtained via *MA*. As is well known, the crystallite size can be comparable to the average crystallite size in nanostructured polycrystalline materials. Deviations in the lattice parameter indicate the dissolution of alloying elements within the lattice, while lattice distortions are associated with the presence of point and linear defects. These defects arise during the *MA* process due to multiple factors, such as local heating, plastic deformation, and the interpenetration of alloy components during the formation of a common solid solution.

Table 2

Structural parameters of the main *BCC* phase of $AlFeCoCrNiNb_x$ powders produced by *MA*

Powder	Crystalline size (nm)	Lattice parameter (Å)	Lattice strain (%)
Nb0	15±7	2.87±0.02	0.19±0.07
Nb0.25	12±6	2.88±0.02	0.25±0.04
Nb0.5	13±7	2.88±0.02	0.42±0.07
Nb0.75	12±5	2.89±0.02	0.61±0.09

The crystallite size in the powders of all alloys ranges from 12 to 15 nm, indicating that the *MA* process resulted in the refinement of both the grain and subgrain structures of the powder particles. The crystallite size value for the *Nb0* alloy is larger than that of the *Nb*-alloyed counterparts. As the *Nb* content increases, the lattice parameter of the solid solution also increases. This is attributed to the fact that the atomic radius of *Nb* (1.46 Å) is significantly larger than those of the primary components (*Fe*: 1.24 Å, *Ni*: 1.24 Å, *Co*: 1.25 Å, *Cr*: 1.30 Å, *Al*: 1.43 Å); consequently, the dissolution of *Nb* into the *BCC* phase causes lattice expansion [16]. According to the literature, the equilibrium solubility of *Nb* in a *BCC* lattice does not exceed a mole fraction of 0.25 [17]. However, under the conditions of severe plastic deformation characteristic of the *MA* process, this solubility can exceed the equilibrium limit. Furthermore, the powders of all alloys exhibit microstrain, which increases with growing *Nb* content (Table 2).

Thus, *MA* of powders for all investigated compositions leads to the formation of a homogeneous material consisting of a primary phase, namely, a common solid solution with a *BCC* lattice and a nanostructured

substructure. The addition of *Nb* at concentrations equal to or exceeding its equilibrium solubility results in the formation of a strengthening *Laves* phase, albeit in insignificant quantities, as inferred from the integral intensity estimates of this phase's peaks on the powder diffraction patterns (Fig. 3). Under severe plastic deformation characteristic of *MA*, the solubility of *Nb* in the common solid solution significantly exceeds the equilibrium limit typical for cast alloys. In arc-melted alloys, segregation during crystallization pushes *Nb* atoms into the remaining liquid phase, causing *Nb*-enriched liquid to solidify as the *Laves* phase [17]. In contrast, during *MA*, where new phases form solely through diffusion processes in the solid state, the dissolution of *Nb* into the common solid solution is energetically more favorable than constructing a new phase with a complex intermetallic lattice [21]. Furthermore, it was noted that not all *Nb* dissolves into the common solid solution; some remains as particles retaining their own crystal lattice. However, since this lattice is also cubic, its diffraction peaks completely overlap with those of the common solid solution on the diffraction pattern. In this scenario, the refined *Nb* inclusions are uniformly distributed throughout the grain structure of the powder.

After *SPS*, the phase composition and structure of the investigated alloys change. The X-ray diffraction analysis (*XRD*) results are presented in Fig. 4, as well as in Tables 3 and 4.

According to the XRD data, during the *SPS* process, the *Nb0* alloy undergoes the following phase transformation: more than half of the volume fraction of the disordered solid solution with a *BCC* lattice reconstructs into an *FCC* lattice. According to the literature, the residual *BCC* phase decomposes into two X-ray indistinguishable components with the same lattice type and similar parameter values: an ordered (*B2*) and a disordered solid solution, denoted as *BCC*/*B2* on the diffraction patterns [22, 24].

In *Nb*-alloyed alloys, alongside the transformation of part of the *BCC* phase into the *FCC* phase, the fraction of the *Laves* phase increases significantly. In the *Nb0.25* alloy, the *Laves* phase constitutes about one-third of the volume fraction, while in the *Nb0.75* alloy, its fraction increases to nearly half the volume (Table 3).

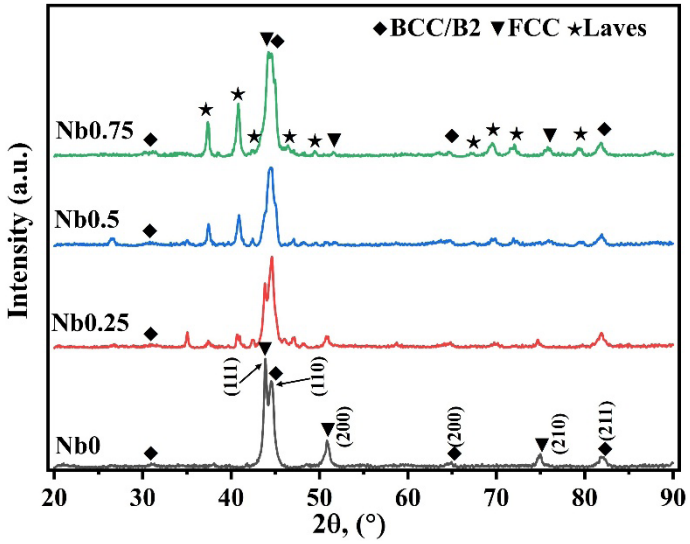

Fig. 4. XRD patterns of $AlFeCoCrNiNb_x$ alloys produced by *SPS*

Table 3

Volume fraction of phases in $AlFeCoCrNiNb_x$ alloys produced by *SPS*

Alloy	*BCC*	*FCC*	*Laves* phase
Nb0	41	59	–
Nb0.25	45	24	31
Nb0.5	31	29	40
Nb0.75	29	27	44

Table 4

Structural parameters of the main phases of *AlFeCoCrNiNb$_x$* alloys produced by *SPS*

Phase	Alloy	Crystalline size (nm)	Lattice parameter (Å)	Lattice strain (%)
BCC	Nb0	68±7	2.87±0.02	1.03±0.06
	Nb0.25	40±8	2.88±0.02	0.95±0.14
	Nb0.5	44±5	2.88±0.02	0.86±0.09
	Nb0.75	48±9	2.89±0.02	0.95±0.09
FCC	Nb0	79±14	3.59±0.05	0.67±0.04
	Nb0.25	124±13	3.59±0.05	0.36±0.01
	Nb0.5	132±13	3.59±0.05	0.78±0.02
	Nb0.75	113±15	3.59±0.05	0.64±0.02

In alloys of all compositions, the lattice parameter of the *BCC* crystal structure remains the same as in the powder state, whereas the crystallite size increases by approximately four times. In the formed *FCC* phase, all alloys exhibit the same lattice parameter, and the crystallite size value is larger than that in the *BCC* phase (Table 4). Consequently, the phase transformations in the alloys are accompanied by restructuring of the substructure but do not lead to significant subgrain growth, preserving the nanoscale dimensions in both the *BCC* and *FCC* phases.

Fig. 5 presents *SEM* images of the microstructure of the *AlFeCoCrNiNb$_x$* alloys after *MA* and *SPS*. Each image highlights zones with distinct structures, and their elemental compositions are provided in Table 5.

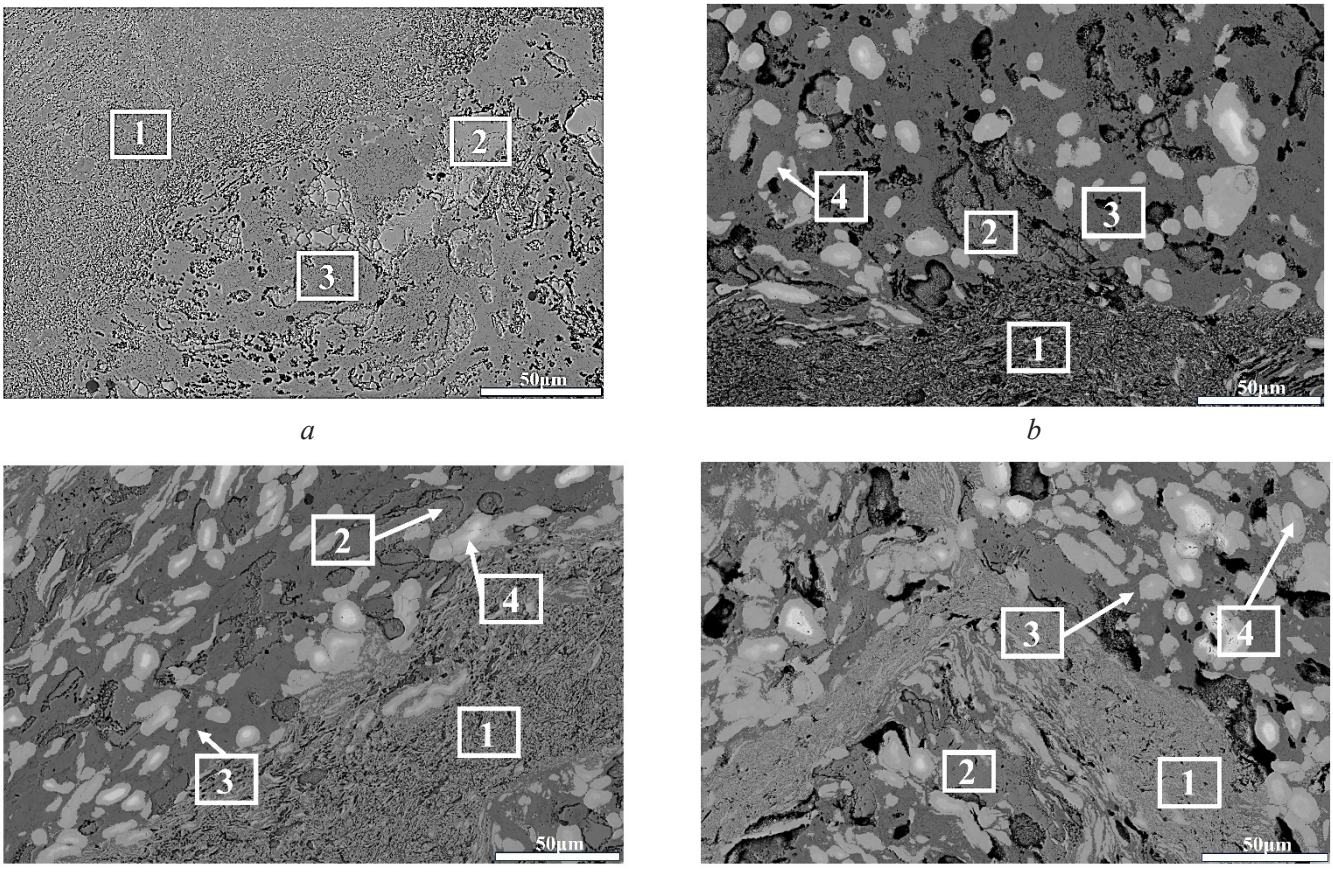

a *b* *c* *в*

Fig. 5. SEM images of the microstructure of *AlFeCoCrNiNb*$_x$ alloys produced by *SPS*:
a – Nb0; *b – Nb0.25*; *c – Nb0.5*; *d – Nb0.75*, where region 1 represents a fine-grained structure; regions 2, 3 and 4 exhibit gray, dark-gray and light-gray contrast, respectively

Table 5

Chemical composition of the structural constituents in *AlFeCoCrNiNb$_x$* alloys produced by *SPS* (at. %)

Structural constituent	Alloy	*Al*	*Cr*	*Fe*	*Co*	*Ni*	*Nb*
Dark-gray contrast	*Nb0*	29.4	9.5	9.6	23.3	28.2	–
	Nb0.25	28.6	9.7	7.9	22.3	30.0	1.5
	Nb0.5	30.5	8.3	9.0	18.6	32.4	1.2
Gray contrast	*Nb0*	4.1	16.0	57.0	14.5	8.4	–
	Nb0.25	5.4	16.9	51.9	15.3	9.8	0.7
	Nb0.5	4.3	11.9	64.1	8.8	10.2	0.7
	Nb0.75	4.3	8.5	76.3	6.0	4.3	0.6
Light-gray contrast	*Nb0*	–	–	–	–	–	–
	Nb0.25	3.7	18.6	9.3	29.9	11.5	27.0
	Nb0.5	3.9	20.8	9.4	28.7	11.5	25.7
	Nb0.75	4.1	23.1	5.3	26.2	13.5	27.8
Fine-grained structure	*Nb0*	22.0	12.9	19.9	22.3	22.9	–
	Nb0.25	27.5	9.9	13.6	18.9	23.2	6.9
	Nb0.5	20.7	13.2	15.8	19.0	21.2	10.1
	Nb0.75	16.5	13.9	18.0	18.7	18.8	14.1

In the *Nb0* alloy, regions with two types of morphology are observed: a fine-grained structure consisting of micron-sized grains (top left corner of Fig. 5, *a*) and areas with a coarse-grained structure composed of structural elements several tens of micrometers in size (bottom right corner of Fig. 5, *a*). The fine-grained structure exhibits two contrast levels: gray and dark gray (region **1**). Zones with the same contrasts also form coarse-grained areas of the structure. There are zones up to 30 μm in size where the gray contrast predominates (region **2**), and zones up to 50 μm where the dark-gray contrast predominates (region **3**). According to the elemental analysis data, all five components of the alloy are present in the grains of both gray and dark-gray contrasts. In the dark-gray contrast zones, there is a tendency to consolidation of *Al*, *Ni*, and *Co*, whereas the grey contrast zones are dominated by *Fe* and *Cr* and have relatively high *Ni* and *Co* content (Table 5). Based on this, it can be assumed that the zones of different contrast represent grains of the two main phases formed during *SPS* from the initial *BCC* solid solution. The zones enriched in *Al* and *Ni* possess a *BCC* lattice, while those enriched in *Fe* and *Cr* have an *FCC* lattice. This conclusion relies on the results of detailed structural studies of an alloy identical in composition and preparation method [16, 29–32]. In this specific alloy composition, the following phases characteristic of a cast structure can form: two general solid solutions with *BCC* and *FCC* lattices, a tetragonal σ phase based on *Cr-Fe-Co*, and an ordered *B2* phase with a *BCC* lattice (*AlNi*). The ratio and type of phases formed during the *SPS* process depend not only on the consolidation regimes but also on the *MA* parameters [31, 32].

According to [29, 32], the phase enriched in *Fe* and *Ni* possesses an *FCC* lattice, which is characteristic for such a composition, as *Ni* acts as a stabilizer for the high-temperature modification of *Fe*. The second phase, with a *BCC*/*B2* lattice, may be a general solid solution containing fine dispersed precipitates of an ordered *B2* solid solution, as described in detail in [22].

Obviously, segregation of components is also present in the areas with a fine-grained structure, caused by the existence of grains with different phase compositions. However, when mapping the elemental composition over an area of several tens of micrometers, the effect of compositional heterogeneity within individual alloy grains is leveled out (Table 5).

Component segregation in individual zones is caused both by inheritance from the *MA* process and by diffusion processes occurring in the material during heating in the *SPS* process. Since *SPS* involves localized heating of specific areas at the boundaries of contacting powder particles, this leads to a gradient temperature distribution within the material volume during compaction. This heating nonuniformity influences the formation of structural heterogeneity in the alloy.

Previous researchers have also noted the characteristic mixed-grain structure (heterogeneous grain size) formed in this alloy during the *SPS* process. The following kinetics of the process is assumed: crystal lattice defects generated during *MA* of the powder, combined with deformation and the high temperature of *SPS*, act as driving forces for dynamic recrystallization followed by the growth of individual grains [22]. As a result, a structure is formed that partially inherits the fine-grained structure of the consolidated powders and partially consists of recrystallized grains.

In the samples of alloys doped with *Nb*, a structure similar to that of the alloy without *Nb* is formed (Fig. 5). Just as in the *Nb0* alloy, regions with two types of morphology are observed in approximately equal proportions: a fine-grained structural component (bottom right corner of Fig. 5, *b*) showing traces of plastic deformation, and regions consisting of large structural elements (top right corner of Fig. 5, *b*), both with and without traces of plastic deformation. The regions of the first type lack clear boundaries and form gradient transitions with regions of the second type, which exhibit an intermediate structure. The structural contrast changes, creating a more distinct pattern in both the fine-grained areas and the areas with larger grains.

In the areas with larger grains, alongside the previously observed grains with gray contrast (region **2**) and dark-gray contrast (region **3**), structural elements with light-gray contrast (region **4**) are formed. Some of the light-gray grains exhibit an internal gradient with an unetched center. These light-gray grains form within the dark-gray grains. In the image areas lacking traces of plastic deformation, the shape of light grains is nearly rounded, indicating their secondary nature. Elemental analysis results showed that the light-gray zones correspond to the *Laves* phase, the dark-gray zones (as in the *Nb0* alloy) to the *BCC* phase, and the gray grains to the *FCC* phase. The areas with a fine-grained structure (region **1**) represent a mixture of all three phases present in the alloy (Table 5).

The distribution of components in the alloys is presented in Fig. 6. A general trend is observed: in areas with a fine-grained structure, the distribution of components, including *Nb*, is more homogeneous due to the refinement of the structural constituents. In areas with a coarse-grained structure, it is evident that *Nb* consolidates within the *Laves* phase.

As described above, in alloys containing *Nb*, the *Laves* phase forms in small quantities already during the *MA* process. Meanwhile, the majority of *Nb* either enters the overall supersaturated solid solution or remains as distinct inclusions within the structure. During *SPS*, local zones of the material are heated; consequently, the system has the opportunity to transition from a nonequilibrium to an equilibrium state via dynamic recrystallization. In this scenario, *Nb* should precipitate from the solid solution to form the *Laves* phase, or the *Laves* phase may form based on grains of the *Nb* solid solution. The nucleation sites for new grains could be the *Laves* phase nuclei already formed during *MA*. Microstructural analysis shows that large grains of the *Laves* phase form within the grains of the *BCC* solid solution. This process depletes the *BCC* matrix of *Nb* while enriching it with *Al* and *Ni*, as these elements are not part of the *Laves* phase, which is described by the general formula $(CoCr)_2Nb$ (Fig. 5, Table 5) . In some particles of the *Laves* phase, contrast-free zones are present in the center. *EDS* analysis reveals that these are solid solutions based on *Nb*, where the *Nb* content is approximately 95 at.%. Thus, it can be hypothesized that large particles of the *Laves* phase form during dynamic recrystallization based on the preserved *Nb* particles, and their growth is sustained by the diffusion of components from the general supersaturated solid solution created during *MA*. It is reasonable to assume that similar mechanisms govern the formation of the *Laves* phase in areas with a fine-grained structure.

It should be noted that the regions of the alloy exhibiting characteristic fine-grained and coarse-grained structures significantly exceed the size of the sintered powder particles. Based on general concepts regarding the kinetics of the *SPS* process, the following mechanism for the formation of such a structure can be hypothesized [33]. Due to the high temperature (1,000 °C) during powder consolidation, the process of plastic deformation proceeds quite intensively, effectively absorbing the original powder boundaries and forming new conglomerates of larger size. On the micrographs, these newly formed structural objects appear as elongated regions with a fine-grained structure inherited from the powder. In areas with the highest concentration of deformation energy, the fine-grained structure is replaced by a coarse-grained secondary structure as a result of recrystallization. However, a more precise description of the kinetics of the material structure formation requires additional research.

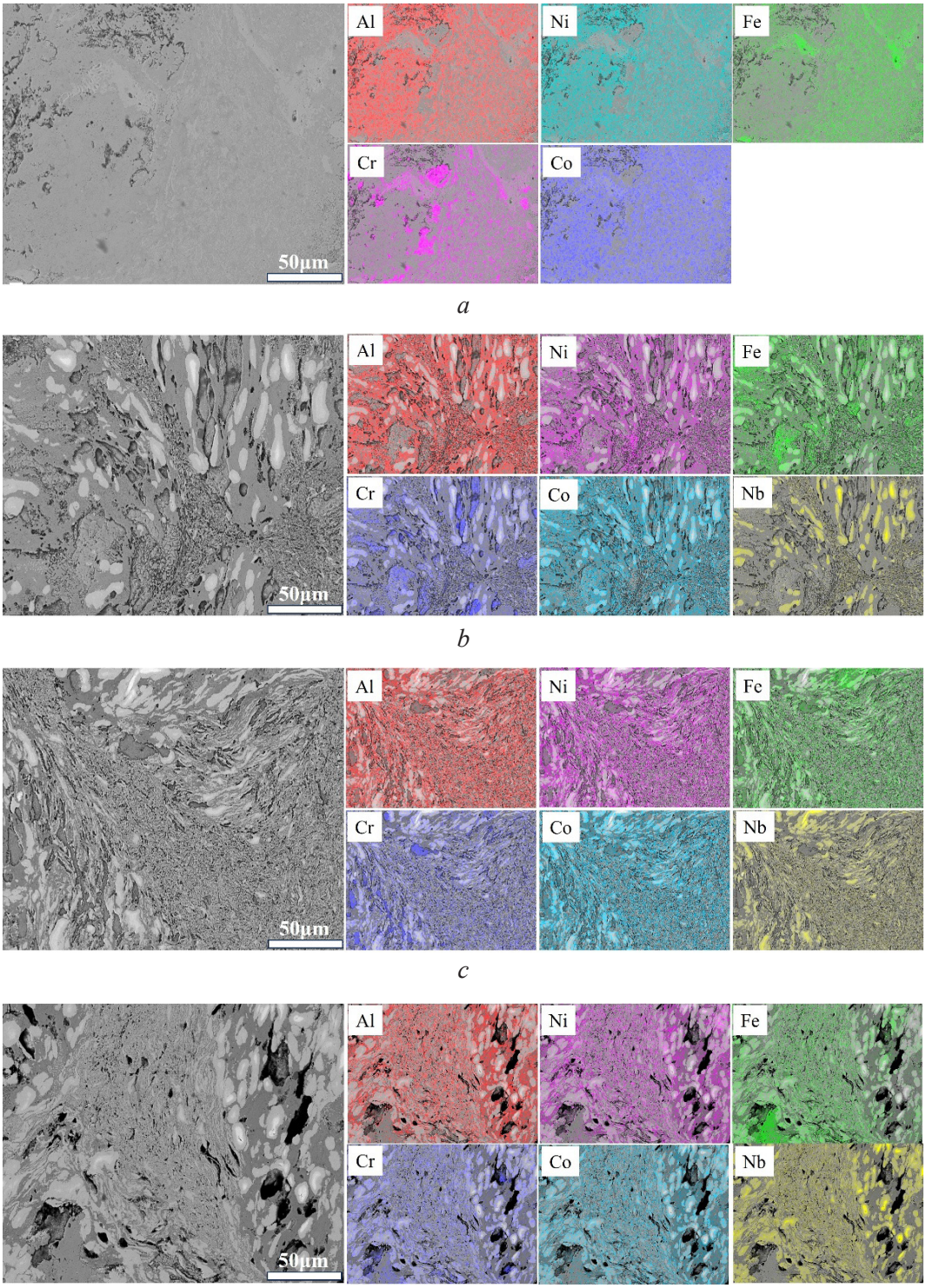

Fig. 6. SEM image and *EDS* results of *AlFeCoCrNiNb*$_x$ alloys produced by *SPS*:
a – Nb0; *b – Nb0.25*; *c – Nb0.5*; *d – Nb0.75*

Microhardness measurements of the investigated alloys revealed that the presence of two distinct microstructural regions with differing morphologies does not induce significant scatter in the obtained values. Although the hardness ranges overlap considerably, a noticeable trend emerges: regions characterized by a fine-grained structure exhibit higher average microhardness. Specifically, in the *Nb0.25* alloy, the fine-grained region displays a microhardness range of 584–771 HV (an average of 663 HV), whereas the coarse-grained region spans 499–712 HV (an average of 614 HV). Given that both the elemental and phase compositions remain constant, this enhancement in microhardness within the fine-grained domains

can be attributed solely to the refined scale of the microstructural constituents. The resultant increase in the grain boundary area effectively impedes dislocation motion, thereby augmenting resistance to plastic deformation.

As the niobium content in the alloy increases, the average microhardness exhibits a corresponding rise (Table 6). In this context, the observed strengthening is primarily attributed to shifts in the phase constitution (Table 3). Specifically, a higher volume fraction of the hard *Laves* phase within the microstructure correlates directly with an elevated bulk microhardness. This trend is consistent across alloys of similar composition fabricated via alternative methods, including arc melting and laser cladding (Table 6) [17, 34].

Table 6

Mechanical properties of *AlFeCoCrNiNb$_x$* alloys produced by *SPS*

Alloy	Production method	σ_u (MPa)	$\sigma_{0.2}$ (MPa)	ε. %	Hardness (HV)	**Literature source**
AlCrFeCoNi	*MA* and *SPS*	2,261.3 ± 106	1,562.1 ± 93	7.2 ± 0.4	559 ± 17	Present paper
AlCrFeCoNiNb$_{0.25}$		2,393.8 ± 117	2,092.7 ± 71	0.9 ± 0.2	629 ± 28	
AlCrFeCoNiNb$_{0.5}$		2,241.2 ± 135	–	–	903 ± 32	
AlCrFeCoNiNb$_{0.75}$		1,028.7 ± 139	–	–	941 ± 30	
CoCrFeNiAl	*MA* and *SPS*	1,907	1,462	11.2	625	[23]
AlCoCrFeNi	*MA* and *SPS*	2,659	2,029	9.1	635 ± 4	[32]
	Induction melting	3,072	1,366	29	504 ± 10	
AlCrFeCoNi	Arc melting	3,531	1,373	24.5	520 ± 11	[17]
AlCrFeCoNiNb$_{0.25}$		3,008	1,959	10.5	668 ± 12	
AlCrFeCoNiNb$_{0.5}$		3,170	2,473	4.1	747 ± 10	
AlCrFeCoNiNb$_{0.25}$	Arc melting	1,962	1,356	7.7	625 ± 28	[18]
AlCrFeCoNi	Laser cladding	–	–	–	557	[34]
AlCrFeCoNiNb$_{0.25}$		–	–	–	662	
AlCrFeCoNiNb$_{0.5}$		–	–	–	784	
AlCrFeCoNiNb$_{0.75}$		–	–	–	789	

Porosity assessments conducted via hydrostatic weighing reveal a modest increase in porosity with rising niobium content. Specifically, porosity increases from 1.9 ± 0.5% in the *Nb*-free alloy to 2.1 ± 0.6%, 4.4 ± 0.6%, and 3.2 ± 0.6% in the *Nb0.25*, *Nb0.5*, and *Nb0.75* alloys, respectively.

Fig. 7 presents compressive stress–strain curves for the *AlFeCoCrNiNb$_x$* alloy system. The *Nb0* alloy exhibits superior ductility. While the *Nb0.25* alloy demonstrates enhanced strength characteristics, it suffers from a concomitant reduction in ductility. In contrast, the *Nb0.5* and *Nb0.75* alloys display virtually no plastic deformation, leading to a marked deterioration in their strength properties. Consequently, increasing the niobium content from 0.25 to 0.75 mol% results in a decline in both compressive ultimate strength and relative elongation. However, the alloy with the highest niobium concentration achieves peak microhardness values, a feature that is likely to confer superior wear resistance (Table 6).

The morphological analysis of fracture surfaces of the compression-tested specimens corroborates the aforementioned mechanical property data (Fig. 8).

The fracture surface of the *Nb0* alloy exhibits features characteristic of ductile failure. Slip bands (fine parallel lines spaced approximately 1 μm apart, oriented according to the grain lattice) and small tear ridges (jagged edges indicating local material resistance prior to final rupture) are visible in Fig. 8, *a*. The *Nb0.25* alloy displays a mixed-mode fracture pattern with a quasi-cleavage surface. Fig. 8, *b* reveals relatively flat cleavage facets (planar areas resulting from instantaneous transcrystalline fracture), which are indicative of

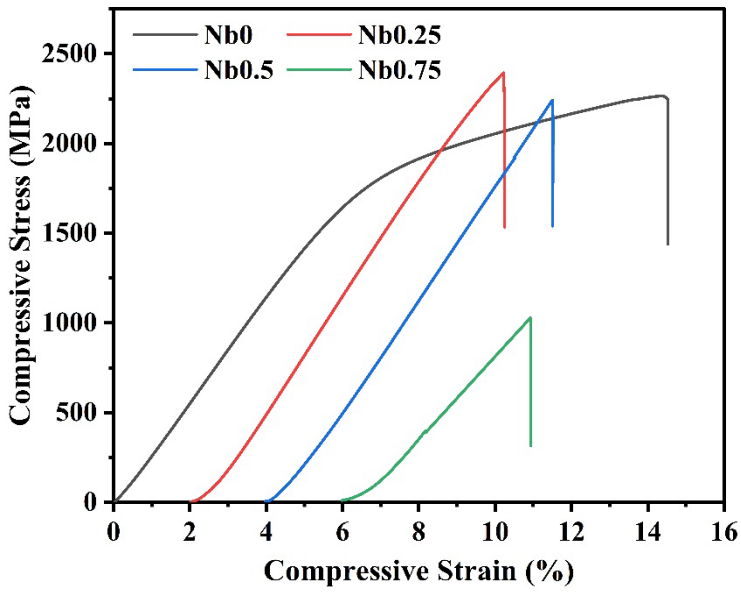

Fig. 7. Compressive stress-strain curves of $AlFeCoCrNiNb_x$ alloys produced by *SPS*

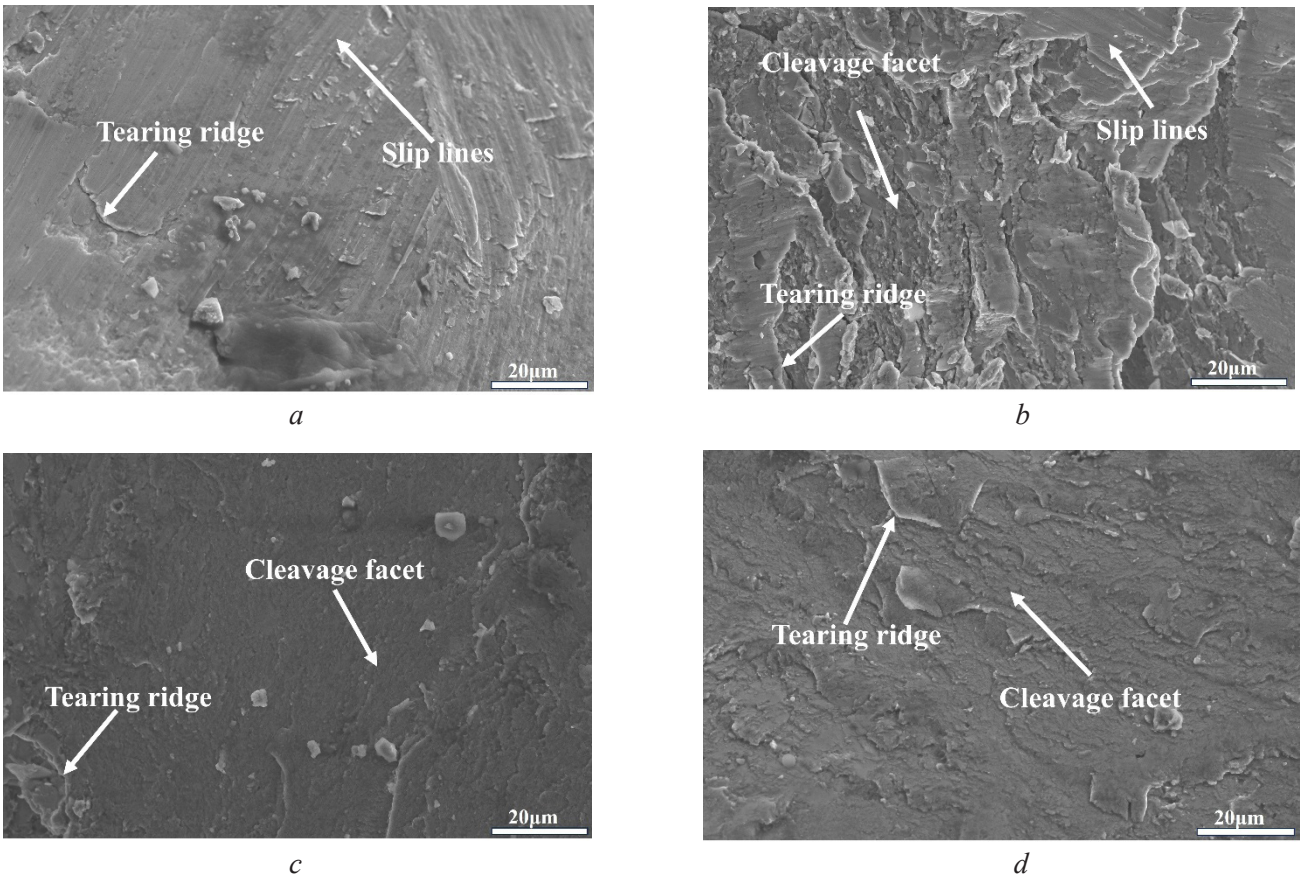

Fig. 8. SEM image of fracture surfaces after compressive tests of $AlFeCoCrNiNb_x$ alloys produced by *SPS*: *a – Nb0*; *b – Nb0.25*; *c – Nb0.5*; *d – Nb0.75*

brittle failure, alongside slip bands characteristic of ductile fracture and tear ridges [23]. In the presented micrograph, the area occupied by brittle fracture features predominates over that with ductile features, consistent with the compressive stress–strain behavior of the *Nb0.25* alloy (Fig. 7). In the *Nb0.5* and *Nb0.75* alloys, which contain a significant fraction of the Laves phase, a brittle fracture mode is observed, which is characterized by smooth, stepped cleavage surfaces and tear ridges (Figs. 8, *c–d*).

Fig. 9 illustrates the correlation between the niobium (*Nb*) content in the investigated alloys, the volume fraction of the *Laves* phase, porosity, and mechanical properties.

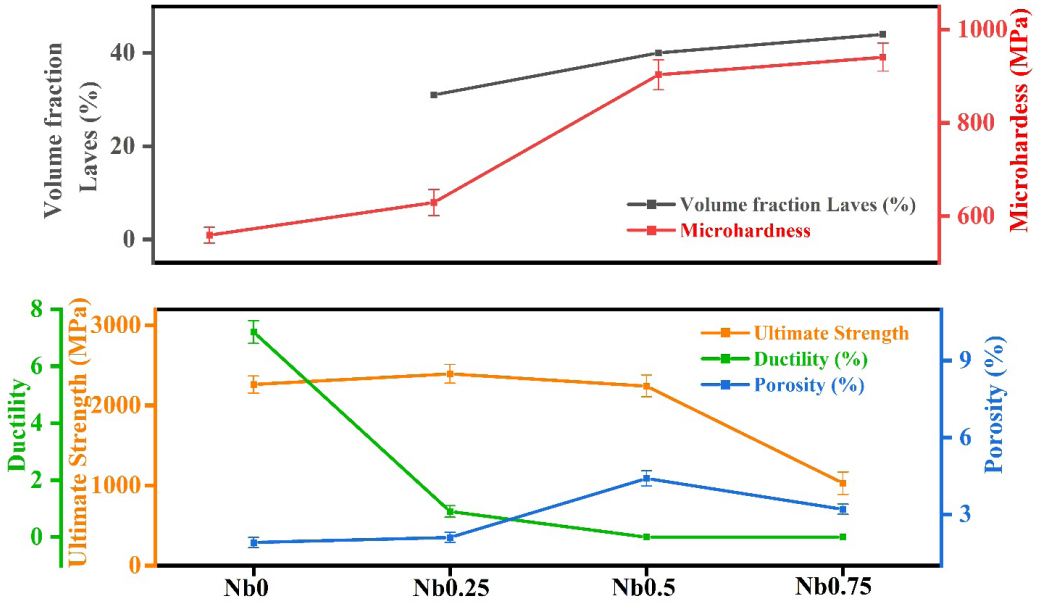

Fig. 9. Correlations between the niobium content in $AlFeCoCrNiNb_x$ alloys, the volume fraction of the *Laves* phase, porosity, and mechanical properties

As shown in the graphs, an increase in the *Laves* phase fraction within the alloy is accompanied by a rise in microhardness, which is concurrent with a reduction in ductility. As previously noted, the strength characteristics are primarily determined by the phase composition and the fracture mode. Additionally, porosity, which increases slightly in the *Nb0.5* and *Nb0.75* alloy samples, can also contribute to reduced strength.

The combination of mechanical properties and the fracture behavior of the $AlFeCoCrNiNb_{0.25}$ alloy synthesized via *MA* and *SPS* makes it a promising wear-resistant material. Possessing a *Laves* phase, a homogeneous fine-grained structure without segregation (unlike cast alloys), and high hardness, this alloy is suitable for friction pairs where bearing steels or cemented carbides fail due to overheating, corrosion, or intense abrasive wear [35–37].

Conclusions

$AlFeCoCrNiNb_x$ high-entropy alloys (*HEAs*) with molar fractions of $\boldsymbol{x}$ = 0, 0.25, 0.5, and 0.75 were consolidated using mechanical alloying (*MA*) combined with spark plasma sintering (*SPS*). During the 40-hour *MA* process, a single-phase solid solution with a body-centered cubic (*BCC*) lattice and a nanosized substructure was formed in the powders of all alloys. Alloying with niobium in amounts exceeding its equilibrium solubility in the matrix phase promoted the formation of a small quantity of the strengthening *Laves* phase within the microstructure.

Subsequent consolidation of the alloy powders via *SPS* under conditions of localized heating up to 1,000 °C facilitated a phase transformation. This resulted in the formation of approximately equal volume fractions of a *BCC* solid solution enriched with *Al* and *Ni* and an *FCC* solid solution enriched with *Fe* and *Cr*.

The microstructure of all alloys consisted of regions with two types of morphology: a mixture of micron-sized grains of all phases, and a structure with grains of the primary phases measuring several tens of micrometers. The heating process promoted the precipitation of the *Laves* phase as secondary grains within the *BCC* solid solution grains. As the *Nb* content increased in the alloy, the volume fraction of the *Laves* phase also increased.

Evaluation of mechanical properties revealed that the *AlFeCoCrNi* alloy exhibited the highest ductility, the $AlFeCoCrNiNb_{0.25}$ alloy demonstrated the highest strength, and the $AlFeCoCrNiNb_{0.75}$ alloy possessed the highest hardness. These variations are attributed to the specific microstructural features and the volume fraction of the *Laves* phase present in each alloy.

References

1. Yeh J.W., Chen S.K., Lin S.J., Gan J.Y., Chin T.S., Shun T.T., Chang S.Y. Nanostructured high-entropy alloys with multiple principal elements: novel alloy design concepts and outcomes. *Advanced Engineering Materials*, 2004, vol. 6 (5), pp. 299–303. DOI: 10.1002/adem.200300567.

2. Cantor B., Chang I.T.H., Knight P., Vincent A.J.B. Microstructural development in equiatomic multicomponent alloys. *Materials Science and Engineering: A*, 2004, vol. 375, pp. 213–218. DOI: 10.1016/j.msea.2003.10.257.

3. Zhang Y., Zuo T.T., Tang Z., Gao M.C., Dahmen K.A., Liaw P.K., Lu Z.P. Microstructures and properties of high-entropy alloys. *Progress in Materials Science*, 2014, vol. 61, pp. 1–93. DOI: 10.1016/j.pmatsci.2013.10.001.

4. Gromov V.E., Konovalov S.V., Efimov M.O., Panchenko I.A., Shlyarov V.V. Puti uluchsheniya svoistv VES Cantor CoCrFeNiMn i CoCrFeNiAl [Ways to improve the properties of high-entropy alloys Cantor CoCrFeNiMn and CoCrFeNiAl]. *Izvestiya vysshikh uchebnykh zavedenii. Chernaya Metallurgiya = Izvestiya. Ferrous Metallurgy*, 2024, vol. 67 (3), pp. 283–292. DOI: 10.17073/0368-0797-2024-3-283-292. (In Russian).

5. Shubert A.V., Konovalov S.V., Panchenko I.A. Obzor issledovanii vysokoentropiinykh splavov, ikh svoistv, metodov sozdaniya i primeneniya [A review of research on high-entropy alloys, its properties, methods of creation and application]. *Obrabotka metallov (tekhnologiya, oborudovanie, instrumenty) = Metal Working and Material Science*, 2024, vol. 26, no. 4, pp. 153–179. DOI: 10.17212/1994-6309-2024-26.4-153-179.

6. Wang W.R., Wang W.L., Wang S.C., Tsai Y.C., Lai C.H., Yeh J.W. Effects of Al addition on the microstructure and mechanical property of Al_xCoCrFeNi high-entropy alloys. *Intermetallics*, 2012, vol. 26, pp. 44–51. DOI: 10.1016/j.intermet.2012.03.005.

7. Chuang M.H., Tsai M.H., Wang W.R., Lin S.J., Yeh J.W. Microstructure and wear behavior of $Al_xCo_{1.5}CrFeNi_{1.5}Ti_y$ high-entropy alloys. *Acta Materialia*, 2011, vol. 59 (16), pp. 6308–6317. DOI: 10.1016/j.actamat.2011.06.041.

8. Liu L., Paudel R., Liu Y., Zhu J.C. Theoretical study on structural stability and elastic properties of $Fe_{25}Cr_{25}Ni_{25}Ti_xAl_{(25-x)}$ multi-principal element alloys. *Materials*, 2021, vol. 14 (4), p. 1040. DOI: 10.3390/ma14041040.

9. Siddiqui D.N., Mehboob N., Zaman A., Alsuhaibani A.M., Algahtani A., Tirth V., Amin M.A. Effect of Cr-doping on the structural and magnetic properties of mechanically alloyed $FeCoNiAlMn_{1-x}Cr_x$ high-entropy alloy powder. *ACS Omega*, 2023, vol. 8 (22), pp. 19892–19899. DOI: 10.1021/acsomega.3c01823.

10. Wang Y.P., Li B.S., Ren M.X., Yang C., Fu H.Z. Microstructure and compressive properties of AlCrFeCoNi high entropy alloy. *Materials Science and Engineering: A*, 2008, vol. 491 (1–2), pp. 154–158. DOI: 10.1016/j.msea.2008.01.064.

11. Manzoni A., Daoud H., Völkl R., Glatzel U., Wanderka N. Phase separation in equiatomic AlCoCrFeNi high-entropy alloy. *Ultramicroscopy*, 2013, vol. 132, pp. 212–215. DOI: 10.1016/j.ultramic.2012.12.015.

12. Tokarewicz M., Grądzka-Dahlke M. Review of recent research on AlCoCrFeNi high-entropy alloy. *Metals*, 2021, vol. 11 (8), p. 1302. DOI: 10.3390/met11081302.

13. Zhou Y.J., Zhang Y., Wang Y.L., Chen G.L. Solid solution alloys of $AlCoCrFeNiTi_x$ with excellent room-temperature mechanical properties. *Applied Physics Letters*, 2007, vol. 90 (18). DOI: 10.1063/1.2734517.

14. Chen J., Niu P., Liu Y., Lu Y., Wang X., Peng Y., Liu J. Effect of Zr content on microstructure and mechanical properties of AlCoCrFeNi high entropy alloy. *Materials & Design*, 2016, vol. 94, pp. 39–44. DOI: 10.1016/j.matdes.2016.01.033.

15. Dong Y., Zhou K., Lu Y., Gao X., Wang T., Li T. Effect of vanadium addition on the microstructure and properties of AlCoCrFeNi high entropy alloy. *Materials & Design*, 2014, vol. 57, pp. 67–72. DOI: 10.1016/j.matdes.2013.12.048.

16. Sunkari U., Reddy S.R., Athira K.S., Chatterjee S., Bhattacharjee P.P. Effect of niobium alloying on the microstructure, phase stability and mechanical properties of $CoCrFeNi_{2.1}Nb_x$ high entropy alloys: Experimentation and thermodynamic modeling. *Materials Science and Engineering: A*, 2020, vol. 793, p. 139897. DOI: 10.1016/j.msea.2020.139897.

17. Ma S.G., Zhang Y. Effect of Nb addition on the microstructure and properties of AlCoCrFeNi high-entropy alloy. *Materials Science and Engineering: A*, 2012, vol. 532, pp. 480–486. DOI: 10.1016/j.msea.2011.10.110.

18. Kovalevskaya Z.G., Liu Y. Vliyanie termicheskoi obrabotki na stroenie i svoistva vysokoentropiinogo splava $AlCoCrFeNiNb_{0.25}$ [Effect of heat treatment on the structure and properties of high-entropy alloy $AlCoCrFeNiNb_{0.25}$]. *Obrabotka metallov = Metal Working and Material Science*, 2025, vol. 27, no. 3, pp. 137–150. DOI: 10.17212/1994-6309-2025-27.3-137-150.

19. Slobodyan M., Pesterev E., Markov A. Recent advances and outstanding challenges for implementation of high entropy alloys as structural materials. *Materials Today Communications*, 2023, vol. 36, p. 106422. DOI: 10.1016/j.mtcomm.2023.106422.

20. Suryanarayana C. Mechanical alloying and milling. *Progress in Materials Science*, 2001, vol. 46 (1–2), pp. 1–184. DOI: 10.1016/S0079-6425(99)00010-9.

21. Vaidya M., Muralikrishna G.M., Murty B.S. High-entropy alloys by mechanical alloying: A review. *Journal of Materials Research*, 2019, vol. 34 (5), pp. 664–686. DOI: 10.1557/jmr.2019.37.

22. Saviot A., Sallamand P., Monchoux J.P., Marcelot C., Cours R., Geoffroy N., Jouvard J.M., Le Gallet S. Phase and microstructure formation during reactive spark plasma sintering of $Al_xCoCrFeNi$ (x=0.3 and 1) high entropy alloys. *Journal of Materials Research and Technology*, 2024, vol. 32, pp. 3047–3059. DOI: 10.1016/j.jmrt.2024.08.096.

23. Ji W., Fu Z., Wang W., Wang H., Zhang J., Wang Y., Zhang F. Mechanical alloying synthesis and spark plasma sintering consolidation of CoCrFeNiAl high-entropy alloy. *Journal of Alloys and Compounds*, 2014, vol. 589, pp. 61–66. DOI: 10.1016/j.jallcom.2013.11.146.

24. Liu X., Gao Y., Peng X., Hu N., Chen M. Phase, microstructure and mechanical properties evaluation of AlCoCrFeNi high-entropy alloy during mechanical ball milling. *Intermetallics*, 2021, vol. 138, p. 107310. DOI: 10.1016/j.intermet.2021.107310.

25. Shivam V., Shadangi Y., Basu J., Mukhopadhyay N.K. Evolution of phases, hardness and magnetic properties of AlCoCrFeNi high entropy alloy processed by mechanical alloying. *Journal of Alloys and Compounds*, 2020, vol. 832, p. 154826. DOI: 10.1016/j.jallcom.2020.154826.

26. Liu G., Lu Z., Zhang X. Nano-structure evolution and mechanical properties of $Al_xCoCrFeNi_{2.1}$ (x = 0, 0.3, 0.7, 1.0, 1.3) high-entropy alloy prepared by mechanical alloying and spark plasma sintering. *Nanomaterials*, 2024, vol. 14 (7), p. 641. DOI: 10.3390/nano14070641.

27. Zhao M., Huang L., Zhang K., Xiong K., Guo D., Feng W. Effect of Nb content on the properties of $Al_{0.1}CoCrFeNi$ high-entropy alloy. *Journal of Materials Research and Technology*, 2025, vol. 37, pp. 5578–5592. DOI: 10.1016/j.jmrt.2025.07.146.

28. Nesterova E.D., Bobkova T.I., Goshkoderya M.E., Kashirina A.A., Yakovleva N.V. Mikroplazmennoe napylenie funktsional'nykh pokrytii iz mekhanicheski sintezirovannykh kompozitsionnykh poroshkov ekviatomnoi sistemy AlNiCoFeCr [Microplasma deposition of functional coatings made of mechanically synthesized composite powders of the AlNiCoFeCr equiatomic system]. *Voprosy materialovedeniya*, 2025, vol. 1 (121), pp. 24–39. DOI: 10.22349/1994-6716-2025-121-1-24-39. (In Russian).

29. Rogal Ł., Szklarz Z., Bobrowski P., Kalita D., Garzeł G., Tarasek A., Szlezynger M. Microstructure and mechanical properties of Al–Co–Cr–Fe–Ni base high entropy alloys obtained using powder metallurgy. *Metals and Materials International*, 2019, vol. 25 (4), pp. 930–945. DOI: 10.1007/s12540-018-00236-5.

30. Mohanty S., Maity T.N., Mukhopadhyay S., Sarkar S., Gurao N.P., Bhowmick S., Biswas K. Powder metallurgical processing of equiatomic AlCoCrFeNi high entropy alloy: microstructure and mechanical properties. *Materials Science and Engineering: A*, 2017, vol. 679, pp. 299–313. DOI: 10.1016/j.msea.2016.09.062.

31. Faraji A., Farvizi M., Ebadzadeh T., Kim H.S. Microstructure, wear performance, and mechanical properties of spark plasma-sintered AlCoCrFeNi high-entropy alloy after heat treatment. *Intermetallics*, 2022, vol. 149, p. 107656. DOI: 10.1016/j.intermet.2022.107656.

32. Kratochvíl P., Průša F., Thürlová H., Strakošová A., Karlík M., Čech J., Cabibbo M. The role of the preparation route on microstructure and mechanical properties of AlCoCrFeNi high entropy alloy. *Journal of Materials Research and Technology*, 2024, vol. 30, pp. 4248–4260. DOI: 10.1016/j.jmrt.2024.04.090.

33. Guyon J., Hazotte A., Monchoux J.P., Bouzy E. Effect of powder state on spark plasma sintering of TiAl alloys. *Intermetallics*, 2013, vol. 34, pp. 94–100. DOI: 10.1016/j.intermet.2012.11.005.

34. Jiang H., Han K., Li D., Cao Z. Synthesis and characterization of $AlCoCrFeNiNb_x$ high-entropy alloy coatings by laser cladding. *Crystals*, 2019, vol. 9 (1), p. 56. DOI: 10.3390/cryst9010056.

35. Chen Z., Luo F., Jin H., Peng Z., Shi W., Huang J. Effect of Nb on laves phase formation and wear resistance in laser-cladding CrFeNi medium-entropy alloy coatings. *Coatings*, 2025, vol. 15 (6), p. 667. DOI: 10.3390/coatings15060667.

36. Hsu C.Y., Yeh J.W., Chen S.K., Shun T.T. Wear resistance and high-temperature compression strength of Fcc CuCoNiCrAl$_{0.5}$Fe alloy with boron addition. *Metallurgical and Materials Transactions A*, 2004, vol. 35 (5), pp. 1465–1469. DOI: 10.1007/s11661-004-0254-x.

37. Zhang A., Han J., Su B., Meng J. Tribological properties of AlCoCrFeNi high entropy alloy at elevated temperature. *Mocaxue Xuebao = Tribology*, 2017, vol. 37 (6), pp. 776–783. DOI: 10.16078/j.tribology.2017.06.008.

Conflicts of Interest

The authors declare no conflict of interest.